Article

Molecular interaction induced dual fibrils towards organic solar cells with certified efficiency over 20%

Chen Chen[1], Liang Wang[1], Weiyi Xia[1], Ke Qiu[2], Chuanhang Guo[1], Zirui Gan[1], Jing Zhou[1], Yuandong Sun[1], Dan Liu[1], Wei Li [1] & Tao Wang [1,2] ✉

The nanoscale fibrillar morphology, featuring long-range structural order, provides abundant interfaces for efficient exciton dissociation and high-quality pathways for effective charge transport, is a promising morphology for high performance organic solar cells. Here, we synthesize a thiophene terminated non-fullerene acceptor, L8-ThCl, to induce the fibrillization of both polymer donor and host acceptor, that surpasses the 20% efficiency milestone of organic solar cells. After adding L8-ThCl, the original weak and less continuous nanofibrils of polymer donors, i.e. PM6 or D18, are well enlarged and refined, whilst the host acceptor L8-BO also assembles into nanofibrils with enhanced structural order. By adapting the layer-by-layer deposition method, the enhanced structural order can be retained to significantly boost the power conversion efficiency, with specific values of 19.4% and 20.1% for the PM6:L8-ThCl/L8-BO:L8-ThCl and D18:L8-ThCl/L8-BO:L8-ThCl devices, with the latter being certified 20.0%, which is the highest certified efficiency reported so far for single-junction organic solar cells.

Organic solar cells (OSCs), as a type of lightweight, flexible, and solution-processable photovoltaics, have shown promising prospects in integrating with wearable clothes, smart electronics and eco-friendly buildings[1–7]. Currently, the cutting-edge OSCs are featured with bulk heterojunction (BHJ) or pseudo-bulk heterojunction (p-BHJ, fabricated by layer-by-layer deposition with BHJ morphology sandwiched with donor- and electron- rich interfacial regions near the electrodes) photoactive layer consisting of electron donor and electron acceptor, in which the photogenerated excitons are dissociated at their interface and the free carriers are transported through their pristine phases toward electrodes[8–10]. However, in solution-processed photoactive layers, the disordered packing networks and undesired phase separation of organic semiconductors usually bring serious charge recombinations, which result in inferior open-circuit voltages (V_{OC}) and fill factors (FF), compared to silicon, perovskite, or other inorganic solar cells[11,12]. Therefore, improving the structure orders and optimizing the nanoscale morphology of organic semiconductors play a critical role in achieving high power conversion efficiency (PCE) of OSCs[8,13–18].

The well-intertwined fibrillar networks of organic semiconductors is considered one of the most suitable morphologies for the photoactive layers of OSC devices, in which the nanofibrils featured with long-range structural order can provide sufficient exciton dissociation interfaces and fast carrier transport channels[8,19–23]. The self-assembly and fibrillization of electron donors and acceptors are primarily driven by the non-covalent interactions between the conjugated backbones of organic semiconductors, thus it could be well mediated by chemical structural design[20,21] and additive engineering[22,23]. Very recently, it was found that, in addition to broadening absorption spectra and manipulating interfacial energetics[24,25], the ternary strategy can also obtain the fibrillar morphology and further improve photon capture and suppress charge recombination, and thereby achieving record efficiencies[8,26–29]. However, the lacking of deep insight into the mechanism of fibril formation, which involves the molecular

---

[1]School of Materials Science and Engineering, Wuhan University of Technology, Wuhan 430070, China. [2]School of Materials and Microelectronics, Wuhan University of Technology, Wuhan 430070, China. ✉e-mail: twang@whut.edu.cn

1

interactions between the third component and host donor or acceptor within the ternary heterojunction, hinders the achievement of new milestone efficiency of 20%.

Here, we designed and synthesized a new non-fullerene acceptor (NFA), namely L8-ThCl, as the third component for the state-of-the-art host system, PM6:L8-BO[19,30,31], and systematically investigate the morphology evolution of both donor and acceptor phases after the introduction of L8-ThCl. We found that the well-arranged edge-on PM6 chains can be twisted into face-on orientation by the dipole–dipole interaction with L8-ThCl, and refined into nanofibrils with enhanced and denser π–π stacks. Meanwhile, the good miscibility and intermolecular interactions between L8-BO and L8-ThCl in W and S-shaped packed dimers can effectively strengthen and regulate the packing networks of acceptors into one-dimension (1D) fibrils with high crystallinity. Employing the layer-by-layer (LbL) deposition method, the enhanced structural order can be retained for both donor and acceptor phases to significantly boost the power conversion efficiency (PCE) of the resulting OSCs. As a result, a PCE of 19.4% was obtained for LbL processed PM6:L8-ThCl/L8-BO:L8-ThCl ternary p-BHJ OSCs and a record PCE of 20.1% was achieved for the D18:L8-ThCl/L8-BO:L8-ThCl ternary p-BHJ OSCs, and the latter was certified 20.0%, which is the highest certified PCE reported so far for single-junction OSCs.

Results and discussion
Materials and fibrillization of donor and acceptor
The chemical structures and energy levels of PM6, L8-BO, and L8-ThCl (with the detailed synthesis routes shown in Supplementary Fig. 1) are shown in Fig. 1a and Supplementary Figs. 2, 3. It can be seen that L8-ThCl shares the same central core with L8-BO, but possesses chlorine-substituted thiophene (2-(1-chloro-6-oxo-5,6-dihydro-4H-cyclopenta[c]thiophen-4-ylidene)malononitrile (CPTCN-Cl)) as end groups, which has been reported to induce stronger intermolecular interaction as well as good compatibility with L8-BO[28,32,33]. This chemical structure feature leads to slightly upshifted energy levels and narrowed full-width-at-half-maxima (FWHM) at its (0-0) absorption peak (Supplementary Fig. 4), not only confirming the stronger aggregation in the film due to stronger intermolecular interaction but also implying that the aligned energy levels might facilitate charge transport in solar cell devices[34].

We first cast thin films of PM6 and L8-BO, with or without adding L8-ThCl, and investigated the interactions between the third component and host donor and acceptor, respectively. From the atomic force microscope (AFM) surface images (Fig. 1b and Supplementary Fig. 5), it is obvious that the weak, thin, and discontinuous PM6 fibrils become denser and continuous after the introduction of more L8-ThCl. These fine and long PM6 nanofibrils remain after chloroform rising to remove any isolated L8-ThCl, taking the one processed with the presence of 20 wt% L8-ThCl as an example (see Supplementary Fig. 5c). Although L8-ThCl in its neat phase will not form fibrils, nanofibrils can also be found in the L8-BO:L8-ThCl (1:0.2) blend film. The 0-0 absorption peak of PM6 in the PM6:L8-ThCl (1:0.2) blend film was also enhanced significantly (Supplementary Fig. 6), which remained strong even after rising with chloroform to remove L8-ThCl, confirming the enhanced structural order of PM6 as a result of strong intermolecular interactions between PM6 and L8-ThCl[35]. A red-shifted absorption peak located at 822 nm was found in the L8-BO:L8-ThCl (1:0.2) blend film, as well as the weakened shoulder peaks, corresponding to enhanced crystallinity and structural order. It was also found that the photoluminescence (PL) peak locations of L8-BO and L8-BO + 20% L8-ThCl films were almost the same, but the intensity of the latter was much higher, indicating the highly mixed phase of L8-BO and L8-ThCl (Supplementary Fig. 7).

According to the two-dimensional (2D) grazing-incidence wide-angle X-ray scattering (GIWAXS) patterns (Fig. 1c), we found the neat PM6 film showed a weak π–π stacking peak at 1.68 Å^{-1} in the out-of-plane (OOP) direction and (100) lamellar peaks at 0.29 Å^{-1} in both in-plane (IP) and OOP directions, corresponding to a mixture of face-on and edge-on orientations of PM6 chains[36]. Interestingly, after adding 20 wt% of L8-ThCl, the intensities of (100) in IP and (010) in OOP both increased, indicating the face-on orientation of PM6 chains (Fig. 1d). While blending with L8-ThCl at 1:1.2 (wt.), the lamellar peak of PM6 in OOP was almost eliminated, the film was dominated by face-on orientation (Supplementary Fig. 8). For NFA and its blend films, L8-ThCl exhibited similar face-on orientation like L8-BO, a π–π stacking diffraction peak locating at 1.74 Å^{-1} (compared to 1.73 Å^{-1} of L8-BO) in OOP was observed, translating to a shortened π–π stacking distance from 3.63 to 3.61 Å (Fig. 2e). When 20% of L8-ThCl was introduced into L8-BO, a red-shifted π–π stacking peak was found locating at 1.79 Å^{-1} with a shoulder at 1.50 Å^{-1}, corresponding to the high crystallinity of NFA conjugated backbones. We also found that the (021) and (11-1) peaks, corresponding to the single crystal lattices of L8-BO, were much more enhanced and independent, as well as the presence of (110) peak, indicating the long-range order and high crystallinity of the L8-BO:L8-ThCl blend film[30,37]. By fitting the 1D profiles of the 2D grazing-incidence small-angle X-ray scattering (GISAXS) images of these pure or blend films, the size and proportion of the crystallized domain of these organic semiconductors can be quantified (Supplementary Fig. 9 and supplementary Table 1). For both PM6 and L8-BO, the introduction of L8-ThCl can significantly enlarge their domain sizes, confirming the strong molecular interactions between L8-ThCl and the host system. According to the SCLC measurements, fibrillization can significantly increase the charge mobilities of both donor and acceptor, which will improve J_{SC} and FF (Supplementary Fig. 10 and Supplementary Table 2).

Theoretical calculations and discussions
Theoretical calculations were performed to understand how L8-ThCl improved the structure order and induced the fibrillization of both donor and acceptor. The density functional theory (DFT) calculation at B3LYP/def2-SVP level was first performed to obtain the optimized single-molecule geometries (Supplementary Fig. 11 and Supplementary Data 1), and the electrostatic potential (ESP) distributions of PM6 and NFAs were well fitted and shown in Supplementary Fig. 12. The ESP distribution of PM6 conjugated backbone is opposite to that of NFAs, which will lead to strong dipole–dipole interaction between adjacent PM6 and NFA molecules[16,36]. Then, molecular dynamics (MD) simulations were performed to simulate the packing behaviors and quantify the intermolecular interactions between L8-ThCl and the host donor and acceptor, with the snapshots of simulated molecular blends at the equilibrium state are shown in Fig. 2a, b. We counted the distance distribution between atoms from different conjugated backbones of PM6, within 4 Å, a general maximum for π–π stackings[38]. It was found that the π–π stacks in the PM6 + 20% L8-ThCl box are more than those in the pure PM6 box (Fig. 2c). Meanwhile, the end-to-end distance and radius of gyration (R_g) of PM6 chains in PM6 + 20% L8-ThCl box are 4.69 and 1.87 nm respectively, shorter than those (5.26 and 2.09 nm) of pure PM6 box (Fig. 2d). This means that with the strong dipole–dipole interaction with L8-ThCl, the PM6 conjugated backbones curved and entangled to form closer π–π stacks (Fig. 2g), which well explains the refined and elongated nanofibrils with structural order in the PM6 + 20%L8-ThCl thin film.

Since the NFAs were reported to form compact packing networks, which are composed of various dimers[22,28], we defined the central core as the D unit and end groups as the A unit and counted their packing ratios (Supplementary Fig. 13)[10]. We found that the ratio of A-A packing, beneficial to prolong the packing network along the length of fibrils[8,22], was increased, while the A-D and D-D packings were reduced, after the L8-ThCl was introduced. Moreover, we noted that the (11-1) and (021) lattices of L8-BO respond to the W shape dimer, and the (110)
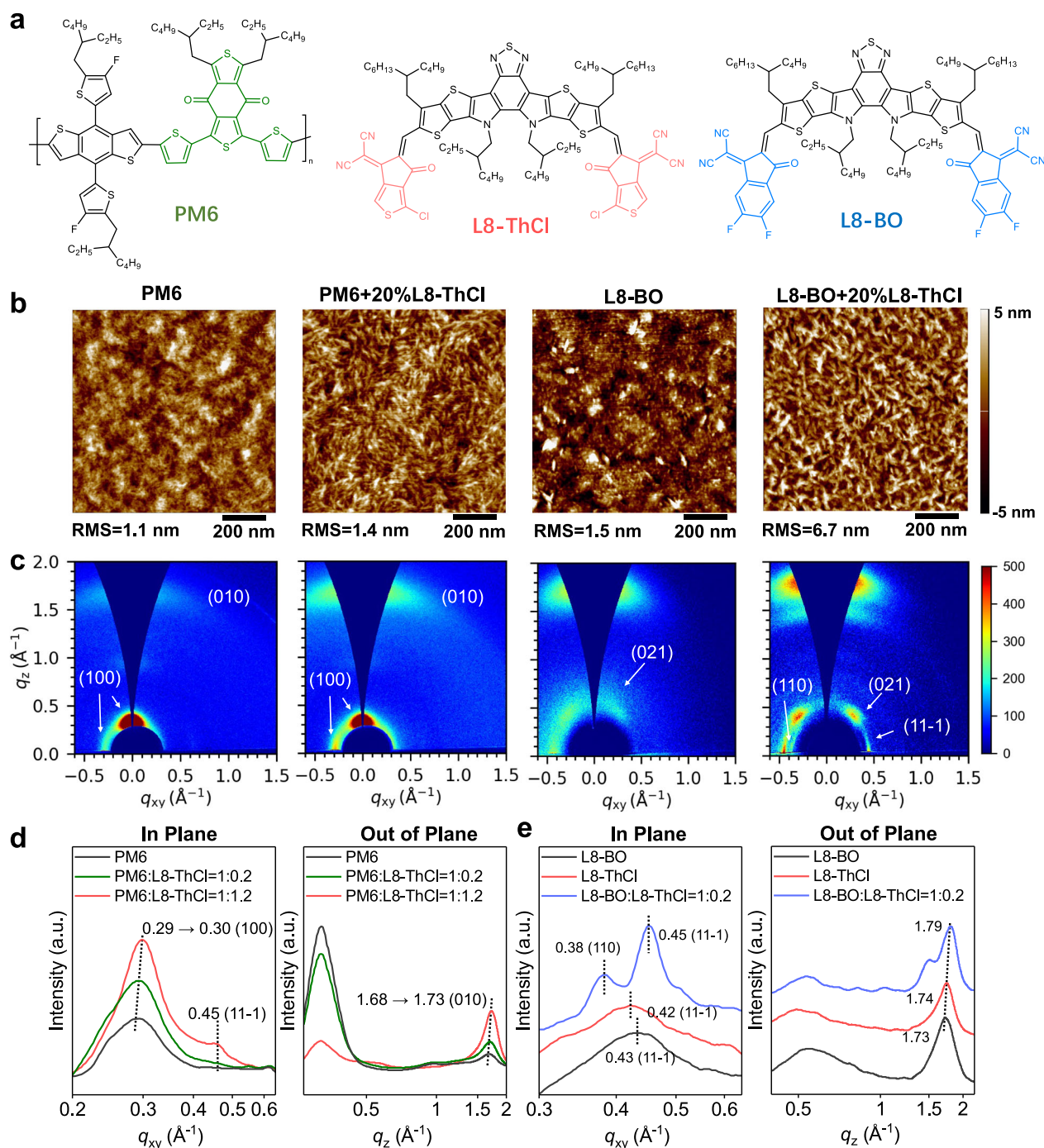
Fig. 1 | Materials and fibrillization of donor and acceptor. a Chemical structures of PM6, L8-ThCl and L8-BO. **b** AFM images of PM6 and L8-BO thin films with or without the addition of 20% L8-ThCl. **c** The 2D GIWAXS patterns of PM6 and L8-BO thin films with or without the addition of 20% L8-ThCl. **d** The 1D GIWAXS profiles of PM6 and PM6:L8-ThCl blends in a thin film state along the IP and OOP directions. **e** The 1D GIWAXS profiles of L8-BO, L8-ThCl, and L8-BO:L8-ThCl blend in a thin film state along the IP and OOP directions. Source data are provided as a Source Data file.

lattice responds to the S shape dimer. Both W and S shape dimers are featured with the overlapping of A units (Supplementary Fig. 14)[21]. It was found that the binding energies of L8-BO to L8-ThCl are greater than those of L8-BO to L8-BO in both W and S shape dimers (Fig. 2f). These results indicate that the interactions between L8-ThCl and L8-BO can strengthen the specific dimers, thus improve the structural order of acceptors and obtain nanofibrils in 1D (Fig. 2h). It was also found the introduction of L8-ThCl can reduce the free volume ratio

(FVR) from 37.7 to 37.1%, a result that may lead to reduced non-radiative energy loss (Supplementary Fig. 15)[39].

Device performance and morphology of binary and ternary OSCs

To validate the advantages of these nanofibrils of both donors and acceptors toward photovoltaic efficiencies, a series of OSC devices were fabricated in a conventional architecture (ITO/PEDOT:PSS/
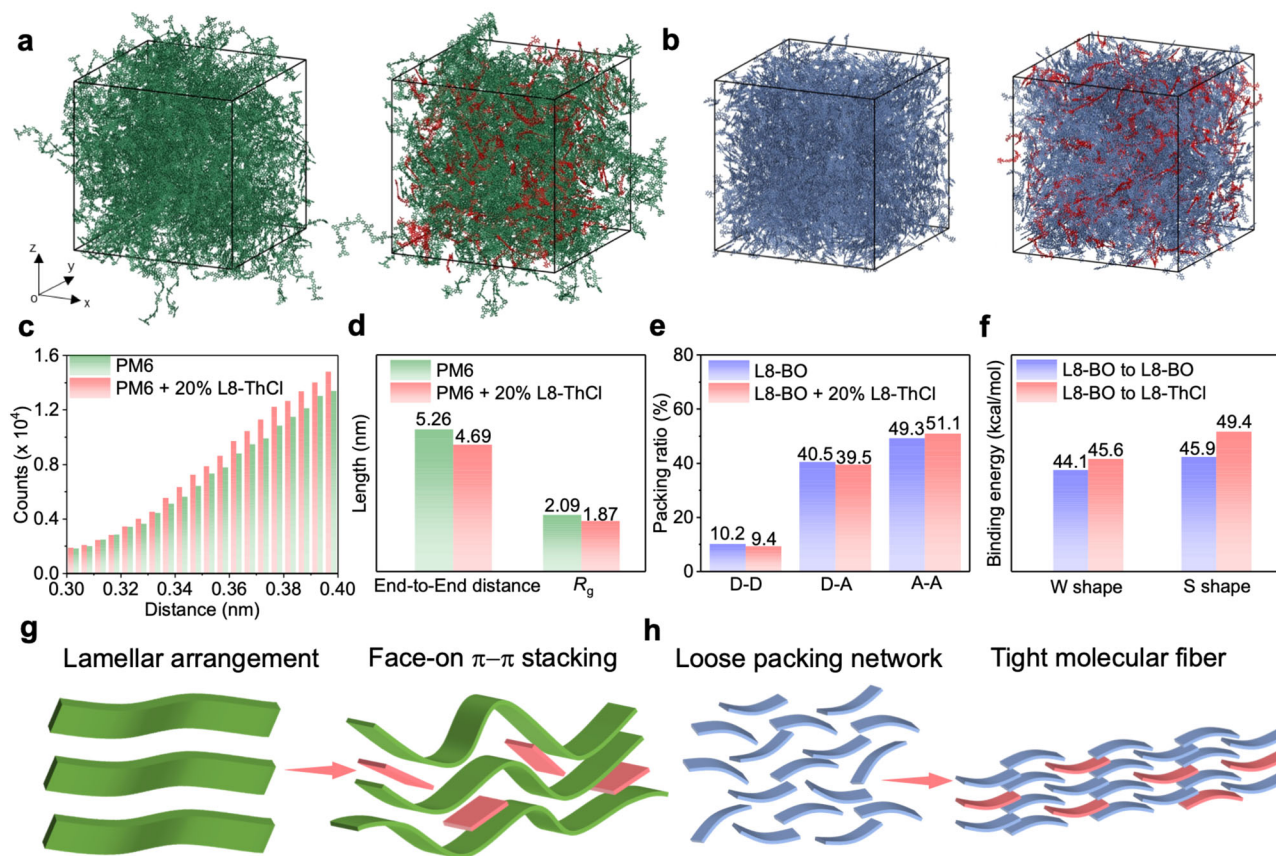
Fig. 2 | Theorical calculation results. The MD snapshots of **a** PM6 box (360 PM6 pentamer chains), PM6 + 20%L8-ThCl box (300 chains of PM6 pentamers and 240 L8-ThCl molecules), **b** L8-BO box (1800 molecules) and L8-BO + 20%L8-ThCl box (1500 L8-BO molecules and 300 L8-ThCl molecules). The PM6 chains, L8-BO and L8-ThCl are colored green, blue, and red, respectively, and all alkyl chains are not shown for clarity. **c** The distribution of distance from different PM6 chains. **d** The calculated end-to-end distances and R_g of PM6 chains in the PM6 and PM6 + 20%L8- ThCl boxes. **e** The ratios of D-D, A-A, and A-D packings in the L8-BO and L8-BO + 20% L8-ThCl boxes. **f** Binding energies of L8-BO to L8-BO and L8-BO to L8-ThCl in W and S -shape packing styles. **g** Illustrations of interactions between PM6 and L8-ThCl, **h** as well as L8-BO and L8-ThCl, in which the long green strips represent the PM6 chain and the short strips represent L8-BO (blue) and L8-ThCl (red). Source data are provided as a Source Data file.

active layer/PDINN/Ag) (Fig. 3a, Table 1, Supplementary Figs. 16, 17, and Supplementary Table 3). As the reference, the PM6:L8-BO binary OSC received a PCE of 18.5% with an FF of 80.6%, consistent with the literature reports[21,30,31], and an inferior PCE of 15.4% with a higher V_{OC} of 0.91 V was obtained for the PM6:L8-ThCl binary OSC. We first mixed PM6, L8-BO, and L8-ThCl directly in the same solution with a weight ratio of 1:1:0.2 to fabricate ternary OSCs with a BHJ photoactive layer. It was found that the ternary BHJ OSC can only slightly improve the PCE to 18.7%. Since the fibrillization strategy had been demonstrated with superior photovoltaic performance in layer-by-layer (LbL) fabricated OSC devices[19,22,23], we further prepared a p-BHJ structured photoactive layer by sequentially casting the PM6 + 20% L8-ThCl and L8-BO + 20%L8-ThCl solutions. As such, a superior PCE of 19.4% was achieved, with all device metrics improved simultaneously (Fig. 3c). The corresponding external quantum efficiency (EQE) spectra are shown in Fig. 3b. All OSCs exhibit higher spectrum intensity above 0.75 across the wavelength range from 450 to 800 nm, and the errors of the integrated current density values and J_{SC} obtained from J-V are within 5%, proving the reliability of device performance. It can be observed that the improvement of J_{SC} in ternary p-BHJ device originates from the enhanced photon response of both donor and acceptor, which is also in good agreement with the absorption spectra (Supplementary Fig. 18). From the Fourier transform photocurrent spectroscopy (FTPS)-EQE spectra, the introduction of L8-ThCl indeed significantly reduced the non-radiative

recombination losses (Supplementary Fig. 19). Furthermore, the transient photovoltage (TPV) and transient photocurrent (TPC) (Supplementary Fig. 20) show that the p-BHJ ternary OSC possess longer carrier lifetime and shorter carrier extraction time, also implying ideal fibrillar networks with optimized structural order that effectively suppressed charge recombination and promoted the photovoltaic performance[40].

We further systematically studied the morphology evolution from binary BHJ to ternary p-BHJ photoactive layers, to better understand the origins of their different photovoltaic performance. According to the AFM images (Fig. 3d), it can be observed that the more distinguished and slenderer nanofibrils were well-distributed on the surfaces of both BHJ and p-BHJ ternary blend films, compared to the pristine PM6:L8-BO film, validating the fibrillization effect of L8-ThCl in ternary systems. The PM6:L8-BO blend films showed a dominant face-on orientation with π-π stacking peak located at 1.73 Å^{-1} with the lamellar peak at 0.30 Å^{-1} in IP (Fig. 3e). For the ternary BHJ blend film, a more profound (11-1) peak locating at 0.45 Å^{-1} in IP was found (Fig. 3f), indicating the enhanced crystallinity of the acceptor phase and confirming the interaction between L8-BO and L8-ThCl. Interestingly, in the ternary p-BHJ blend film, the (100) peaks in the IP direction of PM6 was also significantly enhanced, as well as a stronger π-π stacking peak of both donor and acceptor. The GISAXS results also indicate that the domain size of the acceptor phase can be enlarged in both ternary BHJ and p-BHJ blends, but the domain size of donors only increased in the
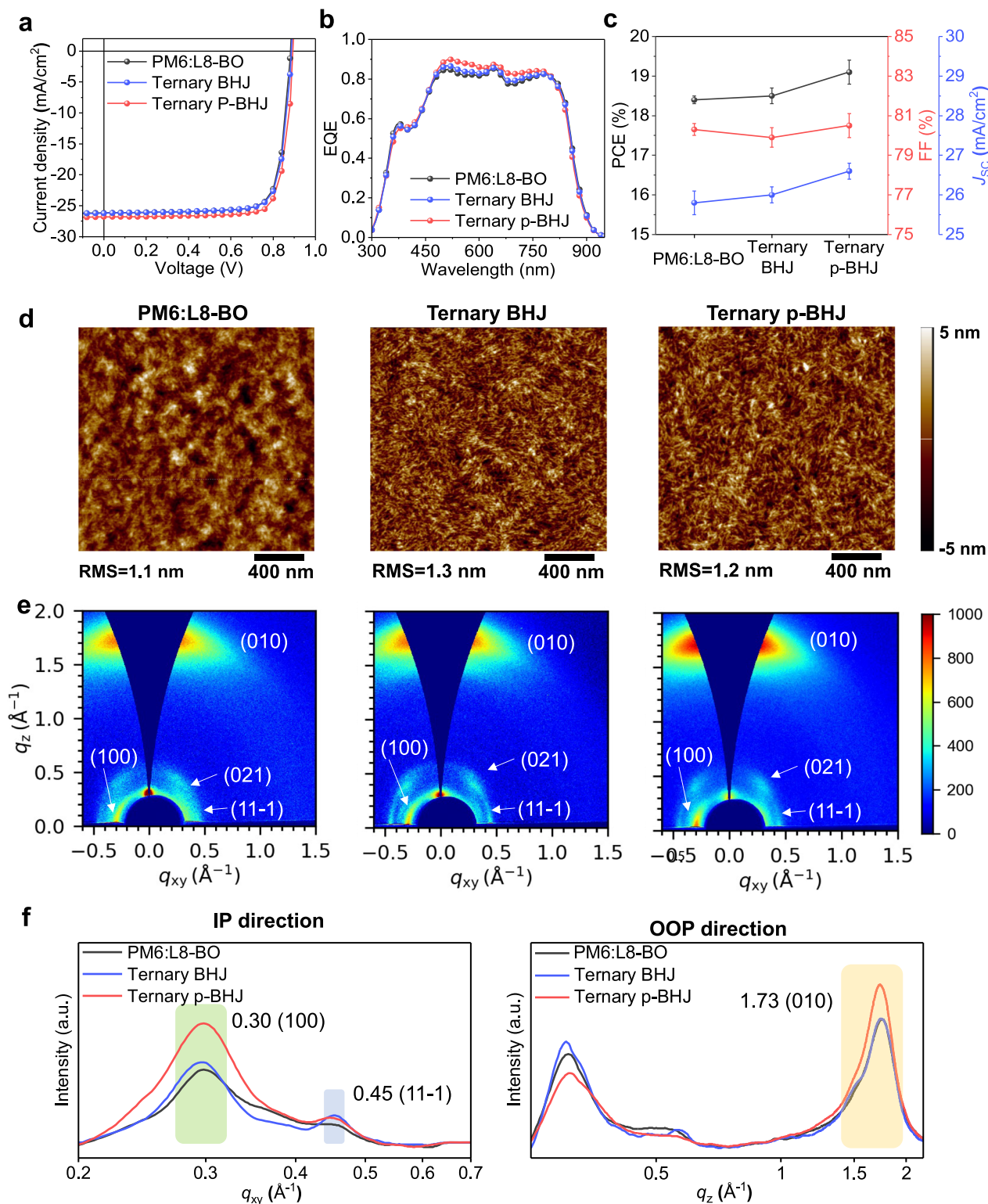
Fig. 3 | Photovoltaic performance and morphology of photoactive layers. a The
J-V curves of PM6:L8-BO based binary and ternary OSCs with **b** corresponding EQE
spectra, and **c** their PCE, FF, J_{SC}, and V_{OC} values. **d** The AFM height images and **e** 2D
GIWAXS patterns of PM6:L8-BO (1:1.2) BHJ, PM6:L8-BO:L8-ThCl (1:1:0.2) BHJ and
PM6:L8-ThCl(1:0.2)/L8-BO:L8-ThCl(1:0.2) p-BHJ ternary active layers, **f** the corre-
sponding 1D profiles along the in-plane (IP) and out-of-plane (OOP) direction.
Source data are provided as a Source Data file.

Table 1 | Summary of device parameters of various OSCs

Active layer	PCE (%)	FF (%)	J_{SC} (mA/cm²)	J_{SC}^{Cal} (mA/cm²)	V_{OC} (V)
PM6:L8-ThCl	15.4 (15.2 ± 0.2)	69.4 (68.9 ± 0.5)	−24.6 (−24.3 ± 0.3)	−23.1	0.911 (0.907 ± 0.003)
PM6:L8-BO	18.5 (18.4 ± 0.1)	80.6 (80.3 ± 0.3)	−26.1 (−25.8 ± 0.3)	−24.9	0.882 (0.880 ± 0.002)
PM6:L8-BO:L8-ThCl Ternary BHJ	18.7 (18.5 ± 0.2)	80.4 (79.9 ± 0.5)	−26.2 (−26.0 ± 0.2)	−25.1	0.889 (0.886 ± 0.003)
PM6:L8-ThCl/L8-BO:L8-ThCl Ternary p-BHJ	19.4 (19.1 ± 0.3)	81.1 (80.5 ± 0.6)	−26.8 (−26.6 ± 0.2)	−25.6	0.895 (0.891 ± 0.004)
D18:L8-ThCl	14.5 (14.2 ± 0.2)	68.8 (68.3 ± 0.5)	−23.2 (−22.7 ± 0.4)	−22.0	0.927 (0.924 ± 0.003)
D18:L8-BO	19.3 (19.2 ± 0.1)	78.7 (78.5 ± 0.2)	−27.2 (−26.9 ± 0.3)	−25.8	0.901 (0.900 ± 0.001)
D18:L8-BO:L8-ThCl Ternary BHJ	19.5 (19.3 ± 0.2)	78.4 (77.9 ± 0.5)	−27.4 (−27.1 ± 0.3)	−26.1	0.904 (0.902 ± 0.002)
D18:L8-ThCl/L8-BO:L8-ThCl Ternary p-BHJ	20.1 (19.8 ± 0.3)	80.3 (79.9 ± 0.4)	−27.5 (−27.3 ± 0.2)	−26.2	0.910 (0.906 ± 0.004)
Certified [a]	20.0	80.5	−27.4		0.907

The average parameters with standard deviation were calculated from 20 individual devices.
Certified at the National Photovoltaic Product Quality Inspection and Testing Center of China.
Source data are provided as a Source Data file.

p-BHJ blend (Supplementary Fig. 21 and supplementary Table 4). The charge mobilities of these films shared the same trend, and the ternary p-BHJ films possessed the highest and most balanced mobilities (Supplementary Fig. 22 and supplementary Table 5). It was also found the PL peaks of these ternary films were closer to the neat L8-BO film, and the quenching in p-BHJ was the most effective (Supplementary Fig. 23). These results imply that the nanofibrils in the ternary BHJ blend film is more likely to correspond to the acceptors phase, while those in the ternary p-BHJ blend film correspond to both donor and acceptor phases.

Here, we calculated the Flory-Huggins interaction parameters of these organic semiconductors by measuring the contact angles of water and ethylene glycol droplets on the neat material substrates (Supplementary Fig. 24 and supplementary Table 6). It was found that the two NFAs, L8-BO and L8-ThCl, showed a very small χ value corresponding to superior miscibility to form molecular co-crystals[28,34,41]. It also implies that in the PM6:L8-BO:L8-ThCl ternary BHJ blends, the merging of L8-ThCl molecules into the L8-BO phase is spontaneous and inevitable, thus the fibrillization of acceptors will be much more remarkable than that of polymer donors. On the other hand, compared with L8-BO, L8-ThCl exhibits better miscibility with PM6, which means it is more suitable as a fibrillization agent for PM6.

Fibrillization of p-BHJ photoactive layer toward 20% efficiency
We further prepared OSCs with another state-of-the-art polymer donor, D18 (Fig. 4a), featured self-assembled nanofibrils, to validate the versatility of our strategy (Fig. 4b-c, Table 1 and Supplementary Figs. 25–27 and Supplementary Table 7, 8)[42–44]. The D18:L8-BO binary OSC realized a PCE of 19.3% with a V_{OC} of 0.901 V, J_{SC} of 27.2 mA cm⁻², and FF of 78.7%, consistent with the literature report[44]. The incorporation of L8-ThCl in the ternary BHJ OSC again brought a minor PCE elevation to 19.5%. Encouragingly, by sequentially depositing the photoactive layer using the D18 + 20%L8-ThCl solution and L8-BO + 20%L8-ThCl solution to form ternary p-BHJ OSC, an unprecedented PCE of 20.1% with the V_{OC} of 0.910 V, J_{SC} of 27.5 mA cm⁻² and FF of 80.3% was achieved. This device obtained a certified PCE of 20.0% at the National Photovoltaic Product Quality Inspection and Testing Center of China (Supplementary Figs. 28–30). To our best knowledge, this is the first case of single-junction OSCs with a certificated PCE of over 20%. The J_{SC} deviations between J-V and EQE measurements are less than 5% too. The longer carrier lifetime and faster carrier extraction calculated from TPV and TPC (Supplementary Fig. 31), respectively, also confirm the better power conversion processes in our championship ternary OSC with a p-BHJ structure. The PL spectra also confirm the most effective charge separation in the p-BHJ film (Supplementary Fig. 32).

The influence of L8-ThCl toward D18 is also evident from the GIWAXS and AFM measurements. The incorporation of 20% L8-ThCl

can also enhance the crystallinity of D18, where the intensities of (100) peak in IP and (010) π−π stacking peak in OOP both increased (Fig. 4e, f), with refined nanofibrils (Supplementary Fig. 33). We notice that, from the ternary BHJ to ternary p-BHJ blends, the crystallinity of both donor phase, associating with the (100) peak in IP, and acceptor phase, associating with the (11-1) and (021) peaks, were increased simultaneously (Fig. 4g, h). Moreover, the (110) peak of L8-BO located at 0.38 Å⁻¹ could be recognized in the ternary p-BHJ film, indicating the promoted structure order of L8-BO fibrils. It was also found that the electron mobility of the ternary p-BHJ film is higher than that of the ternary BHJ film (Supplementary Fig. 34 and Supplementary Table 9). We envisage that the donor phase with a high fibrillization ability, like the case of D18 here, is beneficial for the fibrillization of acceptor in the blend[26], that will further promote the structural order, thus exceptional PCE. Regarding the different solubilities of D18 and PM6, which may lead to different vertical phase separations, the depth-XPS was conducted to quantify the contents of each component of both PM6 and D18-based p-BHJ films (Supplementary Fig. 35). It was found that both PM6 + L8-ThCl/L8-BO + L8-ThCl and D18 + L8-ThCl/L8-BO + L8-ThCl films exhibited vertical gradient for both donors and acceptors, which were beneficial for charge collections[9,14,16].

In this work, we designed and synthesized a new NFA L8-ThCl and employed it as a third component into host photovoltaic blends to form BHJ and p-BHJ ternary OSCs. We found that the incorporation of L8-ThCl into the host donor and acceptor phases independently and casting the photoactive layer via layer-by-layer deposition to form the p-BHJ ternary photoactive layer led to the refined fibrillization of both host donor and acceptor, with fine and long nanofibrils with enhanced structural order and face-on orientation. The molecular dynamics simulations revealed that the PM6 chains can be twisted into closer π−π stacks by the dipole–dipole interactions with L8-ThCl, and on the other hand, the packing networks of L8-BO can be well regulated and elongated into 1D nanofibrils by the intimate interactions with L8-ThCl. As a result, a PCE of 19.4% was obtained for LbL processed PM6:L8-ThCl/L8-BO:L8-ThCl ternary p-BHJ OSCs and a record PCE of 20.1% (certified 20.0%) was achieved for the D18:L8-ThCl/L8-BO:L8-ThCl ternary p-BHJ OSCs. Our strategy offers an encouraging perspective on molecular aggregation manipulation of organic semiconductors to surpass the 20% milestone efficiency of OSCs.

Methods
Materials
PM6, D18, L8-BO, and PDINN were purchased from Solarmer (Beijing), China. PEDOT:PSS (Clevios AI 4083) was purchased from Heraeus, Germany. Other reagents and solvents were purchased from commercial sources and used as received. The synthesis and characterization details of L8-ThCl are provided in the Supporting Information, and Cl-CPTCN were synthesized according to our previous work[28].
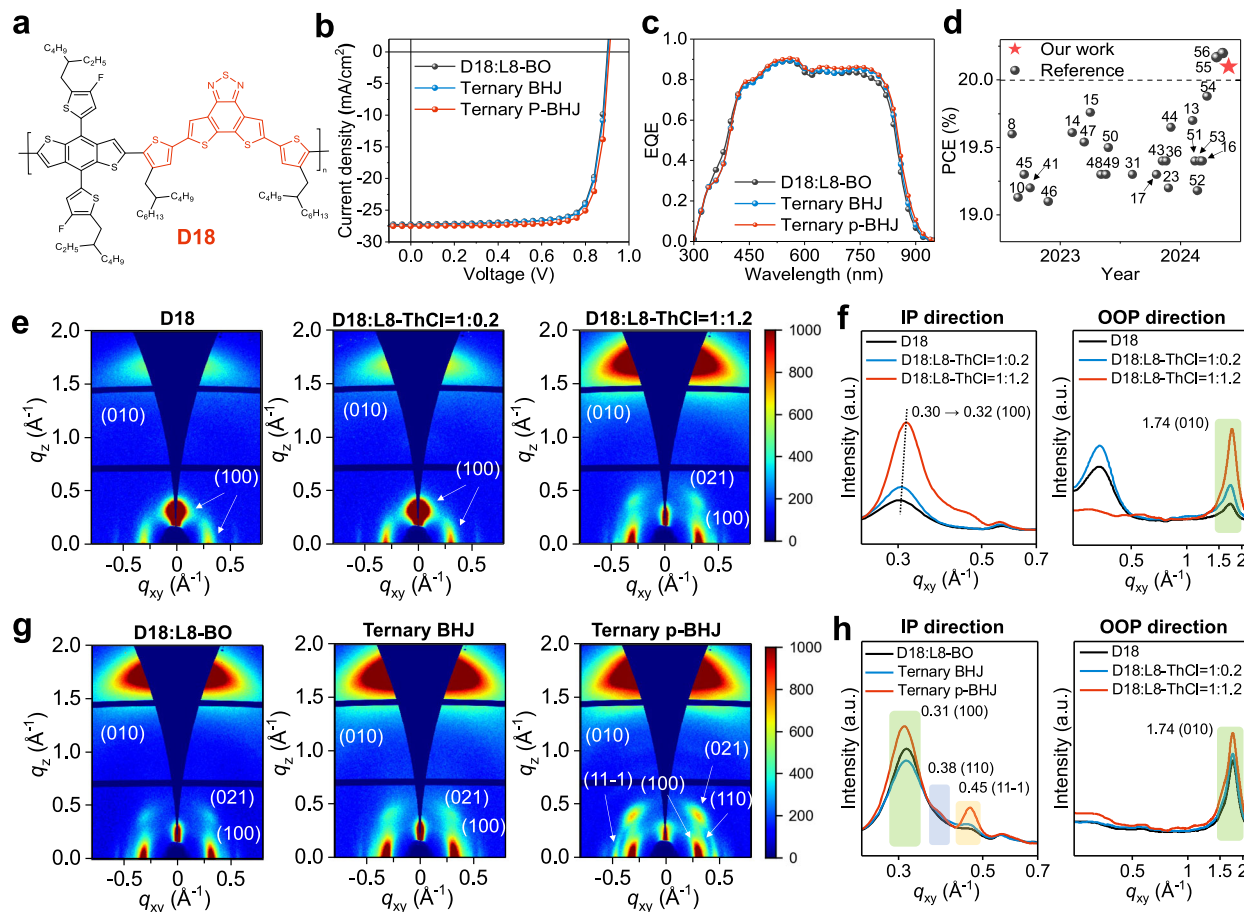
Fig. 4 | Fibrillization of p-BHJ photoactive layer toward 20% efficiency. a The chemical structure of D18. **b** The *J-V* curves and **c** EQE spectra of D18-based OSCs. **d** A summary of single-junction OSCs from literature and this work[8,10,13–17,23,43,44,48–59]. **e** 2D GIWAXS patterns of neat D18, D18:L8-ThCl(1:0.2), D18:L8-ThCl(1:1.2) blend films, **f** the corresponding 1D profiles. **g** 2D GIWAXS patterns of D18:L8-BO (1:1.2) BHJ, D18:L8-BO:L8-ThCl (1:1:0.2), and D18:L8-ThCl(1:0.2)/L8-BO:L8-ThCl(1:0.2) ternary p-BHJ active layers, **h** the corresponding 1D profiles. Source data are provided as a Source Data file.

Solar cell device fabrication

All organic solar cell (OSC) devices were fabricated in a conventional structure (ITO/PEDOT:PSS/active layer/PDINN/Ag). The pre-patterned ITO-glass (resistance ca. 15 Ω per square) were cleaned by sequential sonication in water, ethanol, and isopropyl alcohol for 15 min each. Then these glass/ITO substrates were further treated with ultraviolet/ozone for another 20 min after drying at 150 °C on a hotplate to remove any organic contaminants. About 20 nm PEDOT:PSS films were spin-coated at 5000 rpm on top of the cleaned glass/ITO substrates, followed by thermal annealing at 150 °C for 10 min in air. For BHJ OSC devices, the chloroform solution of the active layer was prepared in a concentration of 15.4 mg/mL, with a mass ratio of 1:1.2 (D:A), and stirred in an N2-filled glovebox overnight. Then, the BHJ active layer with a thickness of around 95 nm was obtained by spin coating at 2500 rpm. As for layer-by-layer (LBL) deposited OSC devices, the organic semiconductors are dissolved in chloroform respectively, with concentrations of 6 mg/mL for PM6, 4 mg/mL for D18, and 8 mg/mL for NFAs. The lower layer was firstly spin-coated from neat polymer donor solution with designed amount of L8-ThCl at 2000 rpm for 30 s to provide thickness of around 46 nm, and the upper layer was then spin-coated from NFA solution (neat L8-BO or L8-BO:L8-ThCl = 1:0.2) at 2500 rpm for another 30 s to obtain a p-BHJ active layer of thickness of around 95 nm. Before spin coating the active layer, 1-bromo-3,5-dichlorobenzen (DCBB) of the same weight with NFA was added as the

additive. Then, both the BHJ and p-BHJ active layers were thermal annealed at 100 °C for 10 min. After that, 1.2 mg/mL PDINN solution was spin-coated at 3000 rpm onto the active layer to afford a 5 nm electron transport layer. Finally, 100 nm Ag were thermally evaporated through a shadow mask under a high vacuum to form the anode. The size of the active area for OSCs defined by the overlapping of anode and cathode is 6.675 mm².

Instruments and measurements

Photovoltaic performance of all OSCs were performed with current density-voltage (*J-V*) sweep software developed by Ossila Ltd. (Sheffield, UK) and a source meter unit (2612B, Keithley, USA). The *J-V* curves of OSCs were measured under AM 1.5 G (100 mW cm⁻²) in the air at room temperature via a Newport 3 A solar simulator, of which the light intensity was calibrated with a standard silicon solar reference cell certified by the National Renewable Energy Laboratory (NREL, USA). An aperture mask was placed over the OSC to accurately define an area of 4 mm² for each pixel. External quantum efficiency (EQE) was measured with a standard Si diode and a Zolix system (China) equipped with the monochromatic beam that was generated using a 150 W xenon lamp. Film thickness was measured using a spectroscopic ellipsometer (J. A. Woollam, USA). The absorption spectra of films were obtained using a UV-visible spectrophotometer (HITACHI, Japan). The surface morphology of all the thin films was measured by an atomic

force microscope (AFM) (Solver Next, NT-MDT, Russia). A Bruker Avance III HD 500 MHz spectrometer was used to characterize the ^1H and ^{13}C NMR spectra of all compounds. Grazing-incidence wide-angle X-ray scattering (GIWAXS) and grazing-incidence small-angle X-ray scattering (GISAXS) measurements were conducted at beamline BL14B1 and BL16B1 at the Shanghai Synchrotron Radiation Facility in China, with a beam energy of 10 keV.

Theoretical calculations

The density functional theory (DFT) calculations were experimented with the ORCA-5.0.4 software package[45], and molecular dynamics (MD) simulations were conducted with the GROMACS 2023 software package with GPU acceleration. The GAFF2 force field was used as an initial parameter. The geometry optimization and single point energy of all single molecules were calculated at the B3LYP/def2-SVP level, and the atomic charges were fitted using the restrained electrostatic potential (RESP) method by Multiwfn software[46]. The dihedral parameters which decide the planerites of conjugated backbones was fitted by scanning the potential energy surfaces at B3LYP-D3BJ/def2-SVP level via Ztop program[47].

The PM6 chains of five repeat units and NFAs were packed in a rectangle box with a size of $40 \times 40 \times 40\ nm^3$ by Packmol software. An annealing run between 500 and 300 K under isothermal-isobaric ensemble (NPT) was firstly performed for five circles in 20 ns. Since the system was well compressed, another NPT run at 300 K in 20 ns was performed to obtain the equilibrated configuration, and the analysis are according to the trajectories in the last 5 ns.

In all of the MD simulations, the V-rescale thermostat and Berendsen barostat were employed to control the temperature and pressure of the system, and the velocity-Verlet integrator at 2.0 fs time step with LINCS algorithm was employed to constrain bonds with hydrogen.

Reporting summary

Further information on research design is available in the Nature Portfolio Reporting Summary linked to this article.

Data availability

All data that support the findings of this study are available within the main text and Supplementary Information file, and also available from the corresponding author on request. Source data are provided with this paper.

References

1. Wang, Z. et al. Self-sustaining personal all-day thermoregulatory clothing using only sunlight. *Science* **382**, 1291–1296 (2023).
2. Li, S. et al. Achieving record-high stretchability and mechanical stability in organic photovoltaic blends with a dilute-absorber strategy. *Adv. Mater.* **36**, 2307278 (2024).
3. Zhang, J. et al. Polymer-entangled spontaneous pseudo-planar heterojunction for constructing efficient flexible organic solar cells. *Adv. Mater.* **36**, 2309379 (2024).
4. Lee, J. et al. Intrinsically stretchable, highly efficient organic solar cells enabled by polymer donors featuring hydrogen-bonding spacers. *Adv. Mater.* **34**, 2207544 (2022).
5. Sun, S. et al. Solution processed semi-transparent organic solar cells over 50% visible transmittance enabled by silver nanowire electrode with sandwich structure. *Adv. Mater.* **35**, 2305092 (2023).
6. Qin, F. et al. 54 cm^2 large-area flexible organic solar modules with efficiency above 13%. *Adv. Mater.* **33**, 2103017 (2021).
7. Chen, H. et al. A guest-assisted molecular-organization approach for >17% efficiency organic solar cells using environmentally friendly solvents. *Nat. Energy* **6**, 1045–1053 (2021).
8. Zhu, L. et al. Single-junction organic solar cells with over 19% efficiency enabled by a refined double-fibril network morphology. *Nat. Mater.* **21**, 656–663 (2022).
9. He, C. et al. Versatile sequential casting processing for highly efficient and stable binary organic photovoltaics. *Adv. Mater.* **34**, 2203379 (2022).
10. Jiang, K. et al. Suppressed recombination loss in organic photovoltaics adopting a planar-mixed heterojunction architecture. *Nat. Energy* **7**, 1076–1086 (2022).
11. Allen, T. et al. Passivating contacts for crystalline silicon solar cells. *Nat. Energy* **4**, 914–928 (2019).
12. Brinkmann, K. O. et al. Perovskite-organic tandem solar cells. *Nat. Rev. Mater.* **9**, 202–217 (2024).
13. Liu, K. et al. 19.7% efficiency binary organic solar cells achieved by selective core fluorination of nonfullerene electron acceptors. *Joule* **8**, 835 (2024).
14. Xu, X. et al. Sequential deposition of multicomponent bulk heterojunctions increases efficiency of organic solar cells. *Adv. Mater.* **35**, 2208997 (2023).
15. Chen, T. et al. Compromising charge generation and recombination of organic photovoltaics with mixed diluent strategy for certified 19.4% efficiency. *Adv. Mater.* **35**, 2300400 (2023).
16. Wang, L. et al. Donor-acceptor mutually diluted heterojunctions for layer-by-layer fabrication of high-performance organic solar cells. *Nat. Energy* **9**, 208–218 (2024).
17. Wen, L. et al. Achieving desired pseudo-planar heterojunction organic solar cells via binary-dilution strategy. *Adv. Mater.* **36**, 2308159 (2024).
18. Campoy-Quiles, M. A universal additive concept yields record-high efficient organic solar cells. *Sci. China Mater.* **67**, 1670 (2024).
19. Li, C. et al. Non-fullerene acceptors with branched side chains and improved molecular packing to exceed 18% efficiency in organic solar cells. *Nat. Energy* **6**, 605–613 (2021).
20. Li, D. et al. Non-fullerene acceptor fibrils enable efficient ternary organic solar cells with 16.6% efficiency. *Sci. China Chem.* **63**, 1461–1468 (2020).
21. Xia, T. et al. Optimal bulk-heterojunction morphology enabled by fibril network strategy for high-performance organic solar cells. *Sci. China Chem.* **62**, 662–668 (2019).
22. Li, D. et al. Fibrillization of non-fullerene acceptors enables 19% efficiency pseudo-bulk heterojunction organic solar cells. *Adv. Mater.* **35**, 2208211 (2023).
23. Liu, C. et al. Alkoxythiophene directed fibrillization of polymer donor for efficient organic solar cells. *Adv. Mater.* **36**, 2308608 (2024).
24. Cui, Y. et al. Single-junction organic photovoltaic cell with 19% efficiency. *Adv. Mater.* **33**, 2102420 (2021).
25. He, C. et al. Manipulating the D:a interfacial energetics and intermolecular packing for 19.2% efficiency organic photovoltaics. *Energy Environ. Sci.* **15**, 2537–2544 (2022).
26. Zhou, J. et al. Bicontinuous donor and acceptor fibril networks enable 19.2% efficiency pseudo-bulk heterojunction organic solar cells. *Interdiscip. Mater.* **2**, 866–875 (2023).
27. Zhang, M. et al. High-efficiency organic photovoltaics using eutectic acceptor fibrils to achieve current amplification. *Adv. Mater.* **33**, 2007177 (2021).
28. Chen, C. et al. Realizing an unprecedented fill factor of 82.2% in ternary organic solar cells via co-crystallization of non-fullerene acceptors. *Adv. Funct. Mater.* **33**, 2305765 (2023).
29. Li, D. et al. Co-crystallization of fibrillar polymer donors for efficient ternary organic solar cells. *ACS Mater. Lett.* **5**, 2065–2073 (2023).
30. Song, J. et al. High-efficiency organic solar cells with low voltage loss induced by solvent additive strategy. *Matter* **4**, 2542–2552 (2021).

31. Guo, C. et al. A polycrystalline polymer donor as pre-aggregate toward ordered molecular aggregation for 19.3% efficiency binary organic solar cells. *Adv. Mater.* **35**, 2304921 (2023).

32. Luo, Z. et al. Reduced energy loss enabled by a chlorinated thiophene-fused ending-group small molecular acceptor for efficient nonfullerene organic solar cells with 13.6% efficiency. *Adv. Energy Mater.* **9**, 1900041 (2019).

33. Luo, Z. et al. Fine-tuning energy levels via asymmetric end groups enables polymer solar cells with efficiencies over 17%. *Joule* **4**, 1–12 (2020).

34. Cai, Y. et al. A well-mixed phase formed by two compatible non-fullerene acceptors enables ternary organic solar cells with efficiency over 18.6%. *Adv. Mater.* **33**, 2101733 (2021).

35. Guo, C. et al. Cold-aging and solvent vapor mediated aggregation control toward 18% efficiency binary organic solar cells. *Adv. Energy Mater.* **11**, 2102000 (2021).

36. Gan, Z. et al. Electrostatic force promoted intermolecular stacking of polymer donors toward 19.4% efficiency binary organic solar cells. *Nat. Commun.* **14**, 6297 (2023).

37. Zhu, L. et al. Efficient organic solar cell with 16.88% efficiency enabled by refined acceptor crystallization and morphology with improved charge transfer and transport properties. *Adv. Energy Mater.* **10**, 1904234 (2020).

38. Li, D. et al. Aggregation of non-fullerene acceptors in organic solar cells. *J. Mater. Chem. A* **8**, 15607–15619 (2020).

39. Jiang, Y. et al. Suppressing electron-phonon coupling in organic photovoltaics for high-efficiency power conversion. *Nat. Commun.* **14**, 5079 (2023).

40. Street, R. A. et al. Photoconductivity measurements of the electronic structure of organic solar cells. *Phys. Rev. B.* **83**, 165207 (2011).

41. Gao, J. et al. Over 19.2% efficiency of organic solar cells enabled by precisely tuning the charge transfer state via donor alloy strategy. *Adv. Sci.* **9**, 2203606 (2022).

42. Liu, Q. et al. 18% Efficiency organic solar cells. *Sci. Bull.* **65**, 272–275 (2020).

43. Lu, H. et al. High-efficiency binary and ternary organic solar cells based on novel nonfused-ring electron acceptors. *Adv. Mater.* **36**, 2307292 (2024).

44. Lu, H. et al. High-pressure fabrication of binary organic solar cells with high molecular weight D18 yields record 19.65% efficiency. *Angew. Chem. Int. Ed.* **62**, e202314420 (2023).

45. Frank, N. Software update: the ORCA program system—version 5.0. *WIREs Comput. Mol. Sci.* **12**, e1606 (2022).

46. Lu, T. et al. Multiwfn: a multifunctional wavefunction analyzer. *J. Comput. Chem.* **33**, 580–592 (2012).

47. Duan, T. et al. Electronic configuration tuning of centrally extended non-fullerene acceptors enabling organic solar cells with efficiency approaching 19%. *Angew. Chem. Int. Ed.* **62**, e202308832 (2023).

48. Zhan, L. et al. Manipulating charge transfer and transport via intermediary electron acceptor channels enables 19.3% efficiency organic photovoltaics. *Adv. Energy Mater.* **12**, 2201076 (2022).

49. Wan, J. et al. An alloy small molecule acceptor for green printing organic solar cells overcoming the scaling lag of efficiency. *Energy Environ. Sci.* **15**, 5192–5201 (2022).

50. Pang, B. et al. Benzo[d]thiazole based wide bandgap donor polymers enable 19.54% efficiency organic solar cells along with desirable batch-to-batch reproducibility and general applicability. *Adv. Mater.* **35**, 2300631 (2023).

51. Li, S. et al. Refined molecular microstructure and optimized carrier management of multicomponent organic photovoltaics toward 19.3% certified efficiency. *Energy Environ. Sci.* **16**, 2262–2273 (2023).

52. Fu, J. et al. 19.31% binary organic solar cell and low non-radiative recombination enabled by non-monotonic intermediate state transition. *Nat. Commun.* **14**, 1760 (2023).

53. Wang, J. et al. Manipulating film formation kinetics enables organic photovoltaic cells with 19.5% efficiency. *CCS Chem.* **6**, 218–229 (2024).

54. Chen, S. et al. Binary organic solar cells with over 19% efficiency and enhanced morphology stability enabled by asymmetric acceptors. *Angew. Chem. Int. Ed.* **63**, e202318756 (2024).

55. Xie, Y. et al. High-reproducibility layer-by-layer non-fullerene organic photovoltaics with 19.18% efficiency enabled by vacuum-assisted molecular drift treatment. *Adv. Energy Mater.* **14**, 2400013 (2024).

56. Zhang, Y. Achieving 19.4% organic solar cell via an in situ formation of p-i-n structure with built-in interpenetrating network. *Joule* **8**, 509–526 (2024).

57. Fu, J. et al. Rational molecular and device design enables organic solar cells approaching 20% efficiency. *Nat. Commun.* **15**, 1830 (2024).

58. Guan, S. et al. Self-assembled interlayer enables high-performance organic photovoltaics with power conversion efficiency exceeding 20%. *Adv. Mater.* https://doi.org/10.1002/adma.202400342 (2024).

59. Sun, Y. et al. π-extended non-fullerene acceptor for compressed molecular packing in organic solar cells to achieve over 20% efficiency. *J. Am. Chem. Soc.* **146**, 12011 (2024).

Acknowledgements

Author contributions

C.C. and L.W. synthesized materials and performed device fabrication, collected data. C.C. conducted molecular dynamics simulations. C.C. and W.X. performed synchrotron X-ray measurements. C.G. and Z.G. conducted optoelectronic measurements. C.C. and K.Q. conducted morphology characterizations. J.Z., D.L., and Y.S. assisted in experimental design and data analysis. All authors were involved in the result discussion. C.C., W.L., and T.W. wrote the manuscript, with all authors commented and revised this paper. T.W. supervised the project.

Competing interests

The authors declare no competing interests.

Additional information

Supplementary information The online version contains supplementary material available at https://doi.org/10.1038/s41467-024-51359-w.

Correspondence and requests for materials should be addressed to Tao Wang.

Peer review information *Nature Communications* thanks Zhenghui Luo and the other, anonymous, reviewer(s) for their contribution to the peer review of this work. A peer review file is available.

Reprints and permissions information is available at http://www.nature.com/reprints

Publisher's note Springer Nature remains neutral with regard to jurisdictional claims in published maps and institutional affiliations.